Transonic Euler Solutions on Mutually Interfering Finned Bodies

Lawrence E. Lijewski*
Air Force Armament Laboratory, Eglin Air Force Base, Florida

The ability of an Euler code to predict mutual aerodynamic interference in the transonic regime was investigated. One-, two-, and three-body combinations of a cruciform-finned configuration were examined at Mach numbers from 0.80–1.20. Predicted surface pressure distributions were compared with wind-tunnel data on three finned bodies. The Euler code was found to predict body pressure well in many interference regions, although shock location often was less accurate due to viscous effects in the strongest interference flowfield near Mach 1. Rigid-body physics of the three-body combination was investigated from integrated pressure distributions. Force and moment behavior was found to be strongly dependent on Mach number.

Nomenclature

C_m = pitching moment coefficient
C_N = normal force coefficient
C_n = yawing moment coefficient
C_p = pressure coefficient
C_{p^*} = sonic pressure coefficient
C_Y = yaw force coefficient
L = lower body
U = upper body
X/C = axial location per local chord length
X/L = axial location per body length
ϕ = angular position

Introduction

IT is widely recognized that the speed, range, and endurance of fighter aircraft is influenced by the aerodynamic forces generated by mutually interfering bodies in external carriage. In addition, the release of these bodies from the parent aircraft is highly dependent on their aerodynamic interrelationship when in close proximity. This influence is most pronounced in the transonic regime where modern tactical fighters often operate. Until recently, it has been difficult to predict numerically the aerodynamic flowfield about mutually interfering finned bodies in the transonic Mach number range. The geometric complexity of the grid generation involved and the existence of embedded subsonic/supersonic flow regions that preclude the use of space marching cones have been major roadblocks to the solution of this problem. With the advent of generalized, arbitrary geometry, multiblock grid codes[1,2] and sophisticated flow solvers[3,4] to work in concert with these grids, good engineering solutions can be obtained on complex configurations.[5,6] Flow calculations have been successfully obtained on multiple unfinned bodies[7,8] and two finned bodies[9] at low angles of attack. Realistic flight conditions dictate the necessity of predicting interference aerodynamics for multiple finned bodies.

The purpose of this paper is twofold: first, to investigate the ability of an Euler code to predict mutual aerodynamic interference, and second, to examine the multibody aerodynamics that occur in the transonic regime when finned bodies are placed in close proximity. Interference effects will be explored by comparing pressure distributions for one-, two-, and three-finned bodies with wind-tunnel data. Force and moment calculations for the three-finned-body case will be examined along with oil flows and pressure distributions to attempt to explain the mutual aerodynamic phenomena occurring between Mach numbers 0.80–1.20.

Configurations

The basic body geometry, Fig. 1, consists of a tangent ogive forebody, cylindrical centerbody, and tangent ogive afterbody, truncated to mount on a sting. Each of the cruciform fins has an NACA 0008 airfoil cross section with exposed aspect ratio of 0.257. The finned body was arranged in one-, two-, and three-body combinations as illustrated in Fig. 2. The separation distance between body centerlines was 1.8 body diameters for both the two-body and three-body configurations. The force and moment convention shown for the single body is identical for the two- and three-body configurations and aligned with the zero angular orientation for each body. The data was obtained in the 4-ft, variable porosity, transonic wind tunnel at Arnold Engineering Development Center, Tullahoma, Tennessee. The configurations were mounted on stings attached to the tunnel main sector, located approximately 2.3 body lengths downstream. To obtain surface pressure data, five 48-port electrically scanned pressure modules were installed and kept at a constant 52°C throughout the test. Pressure data uncertainty was found to be less than 0.7%. Surface pressure data was obtained at 198 pressure taps, which were situated in four longitudinal rows on the body, and two spanwise rows on each of the four fins. The experimental Reynolds number was held constant for all Mach numbers at 2.376×10^6 based on body length. The positive angular orientation is as shown with zero always at the top of each body.

Computational Grids

To obtain accurate flow solutions, a smooth grid must be generated that is as orthogonal as possible. This is a formidable task, considering the complexity of the multiple-body configurations and their close proximity to one another. The grid generation method selected was that of Thompson and Gatlin.[2] This method uses body-conforming coordinate systems to treat arbitrarily shaped boundaries and automatic control functions to achieve desired field grid line spacing and orientation. The grid generator uses a multiblock scheme to handle the geometric complexities. On the multiple-body configuration this approach is imperative, since building one continuous grid that transformed into a single rectangular space would be extremely difficult. To remedy this situation, multiblock grids were constructed for all of the configurations. In addition, although the grids were each built for a different number of bodies, the block construction was made as similar
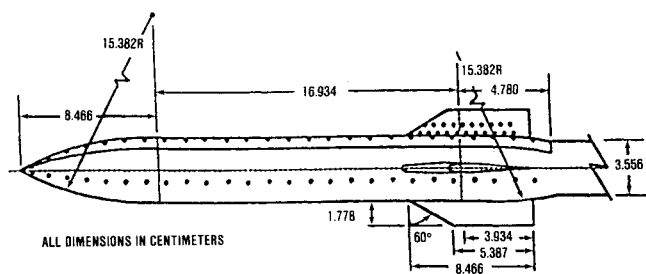
Fig. 1   Finned body geometry

Fig. 2   Configurations

Fig. 3   3-body surface grid

Fig. 4   30-block wireframe grid, 3-body case

Fig. 5   Blocking scheme, 3-body case

as possible to minimize the grid-dependent aspects when comparing calculated pressure distributions.

The most complex configuration was the three-finned body combination, Fig. 3. Since only angle of attack in the vertical plane was to be considered, a symmetry plane existed between the two top bodies, cutting the bottom body in half. The final grid was then constructed for this one and one-half body configuration with a reflection plane to minimize computational costs. The grid was comprised of 30 blocks (275,952 points), with three sections of 10 blocks stacked axially. Figure 4 illustrates the 30-block wireframe grid for the three-body case, outlining the block edges and the three, 10-block sections. The bodies were encased in tube-like grids comprised of a C-O grid from the body stagnation line to the back boundary, and an H-O grid immediately forward of the C-O grid to the front boundary. In this way, 12 blocks formed the grid immediately around the upper body from front to back boundary, while six blocks encompasses the half-body. A cut through the wireframe grid at the fin section, Fig. 5, gives a closer view of how
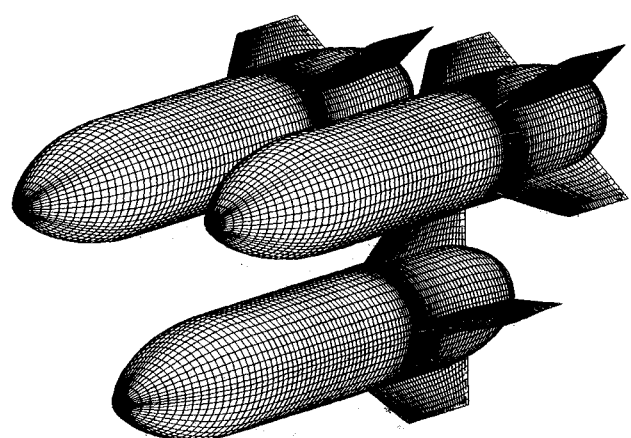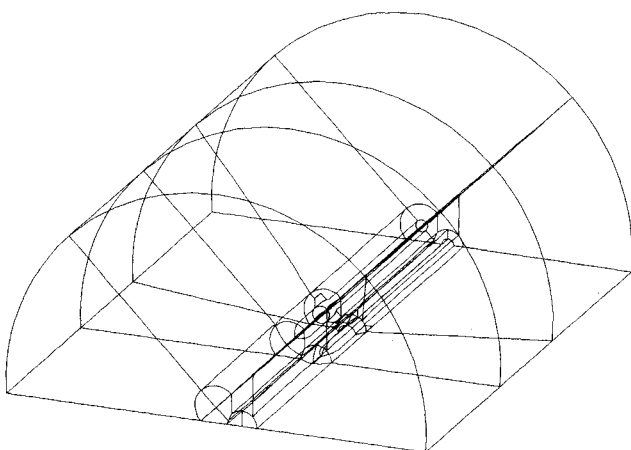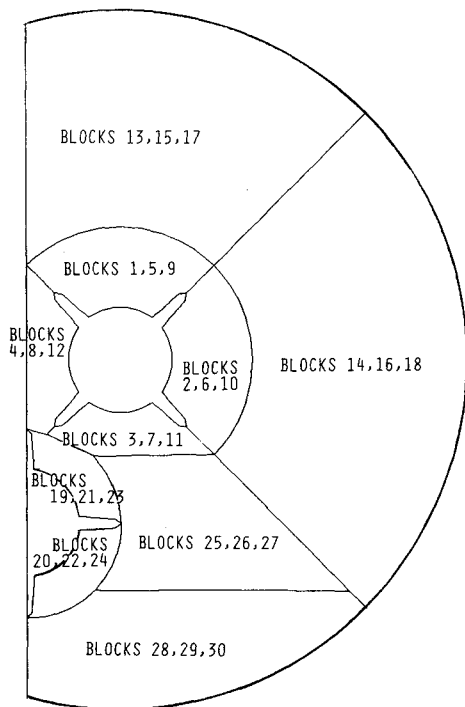
the blocking scheme was formulated. Blocks 1–8 around the upper body were each 10,309 points. Each block was 61 points axially, 13 points radially, and 13 points circumferentially (61 × 13 × 13). Blocks 19–22 around the lower half-body were each 7,930 points (61 × 10 × 13). Twelve larger outer blocks completed the overall grid. Figure 6 gives a three-dimensional perspective of the bodies in relation to the reflection plane, and a cross-sectional grid plane at the back boundary. The tube-like grid construction can be seen around the half-body on the reflection plane as well as the grid around the bodies in the rear plane.

In general, grid line distribution functions were used extensively within individual blocks to achieve smooth transition between blocks. A hyperbolic tangent distribution function was typically used. Nearly uniform spacing was generated on the body forward of the fins, while grid line clustering was used on the fin sections, concentrated at the leading edge. Typical longitudinal cell sizes were 1.2% on the body based on body length and 1.0% on the leading edge of the fins based on

the local chord. The average cell on the fins was 2.6% local chord. The size of the first cell in the normal direction to the body and fin surfaces were typically 3.9% of the body diameter.

As noted earlier, an attempt was made to build all of the grids in a similar fashion. Figure 7 shows the wireframe grid cross section for the two-finned body case, comparable to Fig. 5. The body is again built in a tube-like mesh composed of C-O and H-O grids. The overall grid is now 21 blocks (240,292 points), with three sections of seven blocks each stacked axially. The dimensions of blocks 1–12 are identical to those in the three-body case, with the same grid spacings maintained whenever possible. The wireframe grid cross section for the single-body configuration is shown in Fig. 8. This grid is composed of 24 blocks (289,432 points), and is generated by adding three outer boundary blocks where the reflection plane was located in Fig. 7. Here the size of the first 21 blocks are the same as before with the same spacing enforced where possible.

Computational Results

The flow solver used was the Euler code developed by Belk and Whitfield.[4] The solver is an implicit, two-pass, upwind
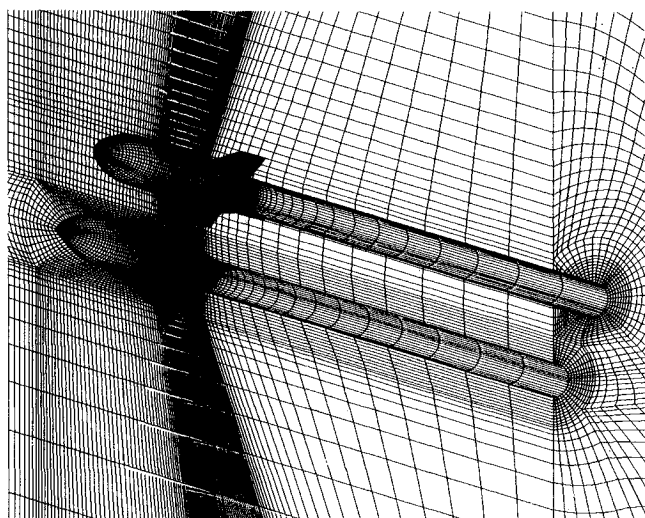

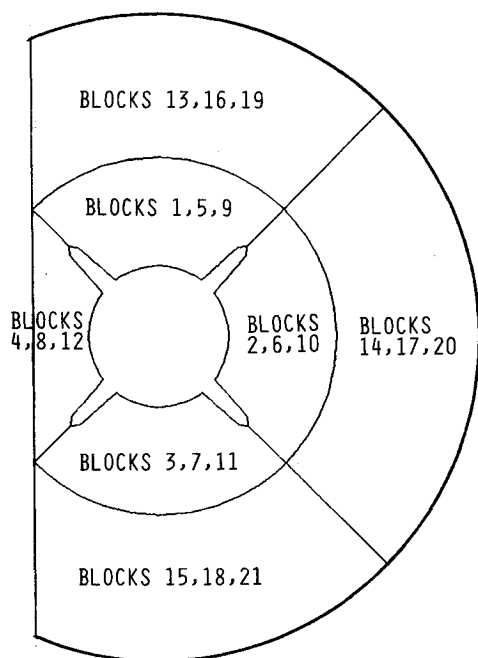Fig. 6   Reflection and back planes, 3-body case

Fig. 8   Blocking scheme, 1-body case
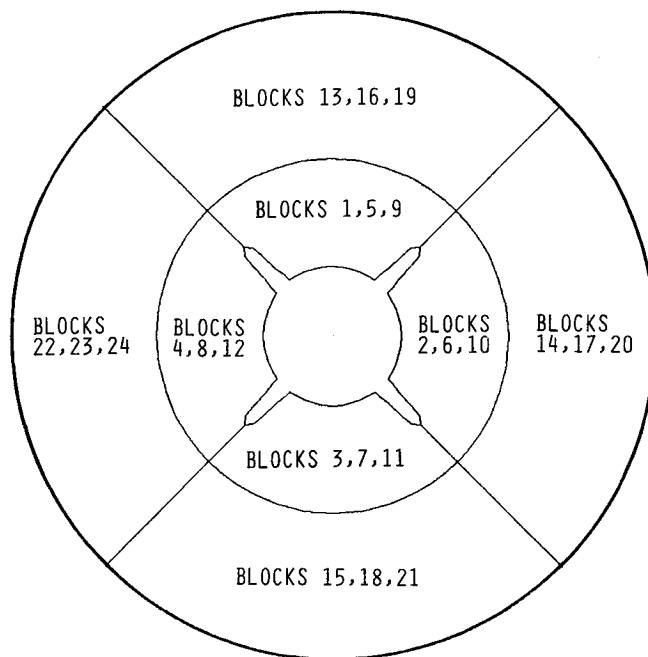

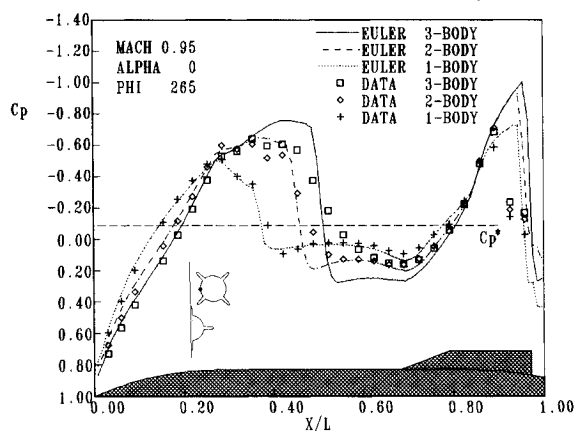Fig. 7   Blocking scheme, 2-body case

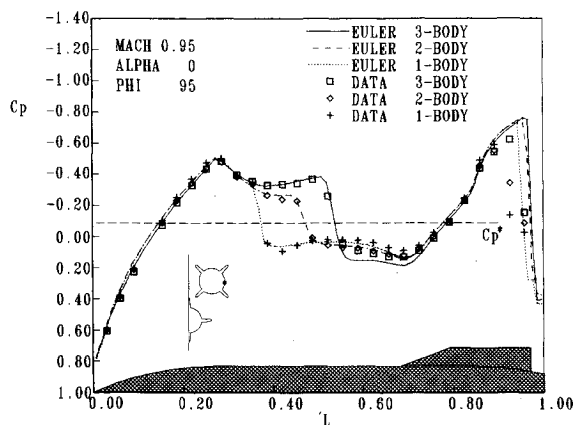Fig. 9   Configuration effects, upper body, inboard side

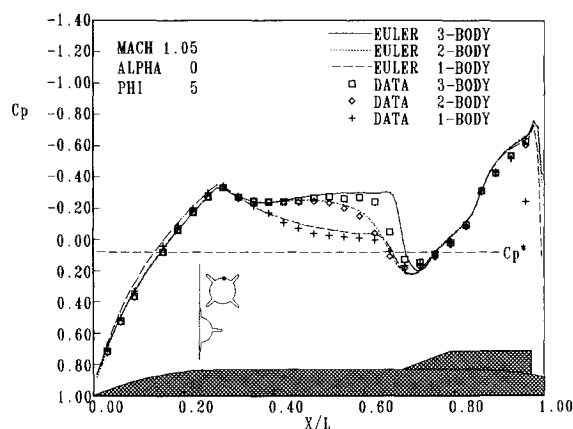Fig. 10   Configuration effects, upper body, outboard side

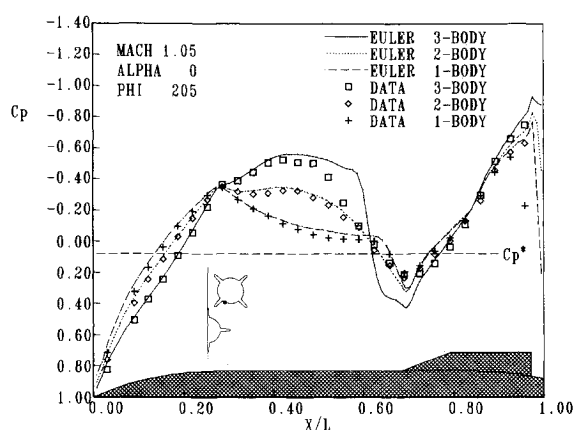Fig. 12   Configuration effects, upper body, upper side

Fig. 11   Configuration effects, upper body, lower side

scheme, third-order accurate in space. It solves the flux-difference-split form of the Euler equations using a modified Roe scheme that is stable for a wide range of Courant numbers for steady-state computations. Characteristic variable[10] boundary conditions were applied on all boundaries. These boundary conditions were used since they efficiently pass information into and out of the computational domain with minimum reflection of flow discontinuities such as shocks. This was important since the inflow, outflow, and far-field boundaries ranged from only 2.1–2.4 body lengths from the configurations. Euler solutions were obtained at Mach numbers from 0.80–1.20 at 0-deg angle of attack. All cases were run to convergence at a Courant number of 5 for 1000 iterations with a speed of approximately 4.9×10^{-5} s/pt/iteration on a CRAY-2 supercomputer.

Multibody Pressure Comparisons

To illustrate the aerodynamic interference in the multibody cases, Fig. 9 plots the pressure coefficients on the inboard side of the upper body for the three-finned configurations at Mach 0.95 and 0 deg angle of attack. It is clear that by adding a second body and then a third, the flow accelerates between the bodies as indicated by the increasing expansion peaks, both on the forebody and between the fins. Also, the expansion regions increase in size, resulting in the shocks moving downstream. It is interesting to note that the expansion rise on the ogive nose generally reaches the same magnitude at the ogive-cylinder junction, $X/L = 0.28$, for all three configurations even though the rate of expansion for each case is different. The Euler code gives very good agreement with data in the one- and two-body cases, even though the interference effects

are strong in the two-body case. The Euler code, however, shows a crisp shock on the body at $X/L = 0.45$ in the two-body case, whereas the data begins to indicate the effects of viscosity and a more smeared shock. This becomes even more evident when the third body is added. Although the data do not show a large difference in the expansion on the cylinder, the flow solver indicates a significant expansion change. Here again the flow solver predicts a sharp shock at $X/L = 0.50$, which is in contrast with the smeared shock indicated by the data. Also, the Euler prediction overcompresses after the shock, unlike in the one- and two-body cases, where the predictions and data more nearly agree after the shock. It is becoming evident from the Euler/data comparisons that the three-body case is much more viscous dominated than the two-body case. Finally, in the fin region, the expansion and subsequent shock is overpredicted and downstream as would be expected from an Euler code. However, the fin region is highly viscous, near Mach 1.0, as will be discussed later.

In contrast to the inboard side of the upper body, the outboard side, Fig. 10, is much better predicted, even in the fin region. The main interference effect here is the elongation of the expansion region near midbody with the subsequent rearward movement of the shock, as the second and third bodies are added. In all three cases, the flow solver does quite well. Interference effects are not felt on the outboard side of the ogive nose, compared to what was seen on the inboard side. In fact, the pressure distribution on the outboard side of the body in the multibody cases closely resembles the distribution for the single-body case, except for the shock location. Therefore, the interference flowfield shock formed on the body is not a local phenomenon on the inboard side of the body, but rather a shock disk extending around to the outboard side. The strength of the shock may vary from the inboard to the outboard side, but the outboard shock location is similar to the inboard shock location.

Supersonically at Mach 1.05, Fig. 11, the shock on the body does not make a dramatic rearward movement as the second and third bodies are added. The significant interference effects are the pressure expansion region growth and acceleration of the flow on the inboard side, as the second and third bodies are added. Even though the angular location, $\phi = 205$ deg, is on the bottom side of the upper body, the addition of the second body produced a significant pressure expansion increase. Here also the expansion rise on the ogive nose behaves similarly to that at Mach = 0.95, reaching the same magnitude at $X/L = 0.28$ for all three cases.

Figure 12 illustrates the good agreement on the top side of the upper body. Here again the data shows little change in the shock location as additional bodies are added, although the magnitude of the expansion increases. With this body location being the farthest from the third body, the relatively small increase in flow expansion is not surprising.

Multibody Aerodynamics

When investigating the aerodynamic interference phenomena of multiple bodies in close proximity, the question arises as to the mutual aerodynamics of such configurations. How the bodies react to each other and the underlying causes of the reaction are important to understand. The pressure distributions are integrated for the three-body configuration to obtain the force and moment coefficients from Mach 0.80–1.20. Figure 13 plots the normal and side forces of the upper body and normal force of the lower body. Figure 14 plots the pitching and yawing moments of the upper body and the pitching moment of the lower body. The moment reference center is located at $X/L = 0.561$. The axis system and sign convention from Fig. 2 is in effect here for both the upper and lower bodies. Up and down refer to the vertical axis, while in and out refer to the horizontal axis in Fig. 2.

What is evident immediately from Fig. 13 is that the forces on the bodies tend to move the bodies together in subsonic flow, but move the bodies away from each other at supersonic Mach numbers. The inward forces at Mach 0.80 also appears to be significantly stronger than the outward forces at Mach 1.20. Here inward and outward refer to the direction from the center of the configuration. Figure 15 illustrates this strength by comparing the pressure distributions on the inboard and outboard sides of the upper body at Mach 0.80. The outboard side prediction is at 85 deg clockwise from top center, while the inboard side prediction is at 265 deg. The two expansion regions on the inboard side at the nose and tail provide a strong inboard force when compared to the same two outboard locations. This identical pattern was also observed on the upper/lower sides of both the upper and lower bodies,

where the expansion peaks on the maximum interference sides determined the force direction. The result was an inward/downward force on the upper body and upward force on the lower body. Supersonically, the forces reverse themselves. The pressure distribution on inboard and outboard sides of the upper body, Fig. 16, give evidence for this reversal. In marked contrast to Mach 0.80, the flow expansion in the fin region is similar from one side of the body to the other. In addition, the pressure on the outboard side of the nose expands more rapidly than the inboard side, resulting in a net outboard force. However, the significant contributions to the outward force occurs as a result of the shock on the body near
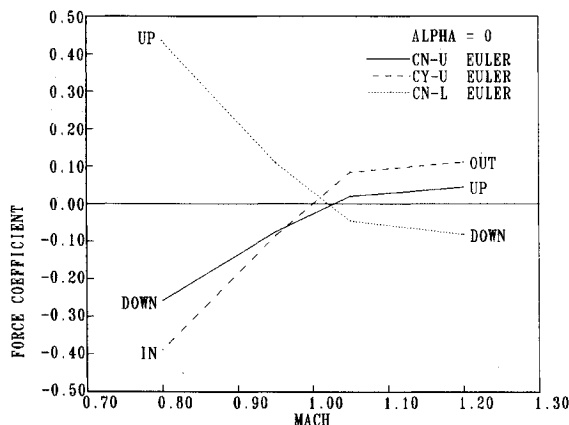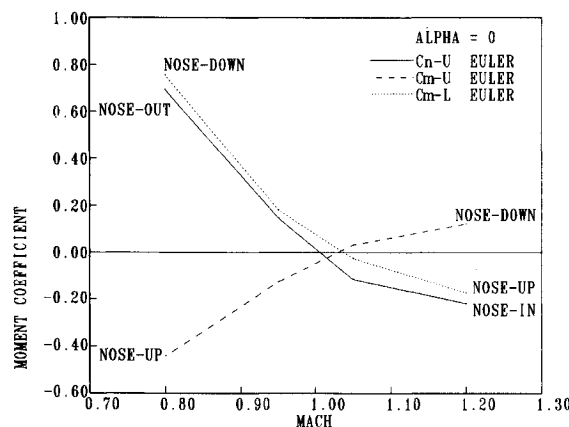
Fig. 15   Subsonic interference effects, upper body

Fig. 13   Force coefficients, 3-body case

Fig. 16   Supersonic interference effects, upper body

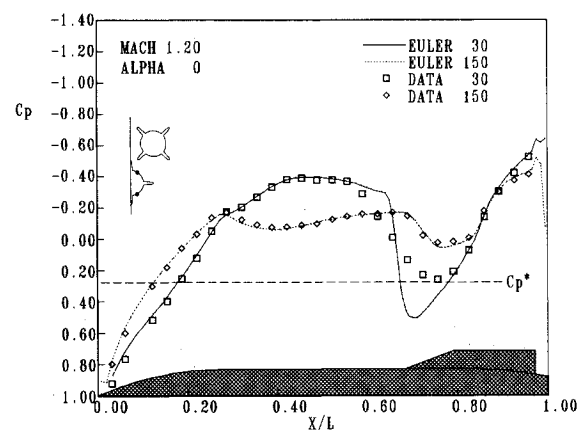Fig. 14   Moment coefficients, 3-body case
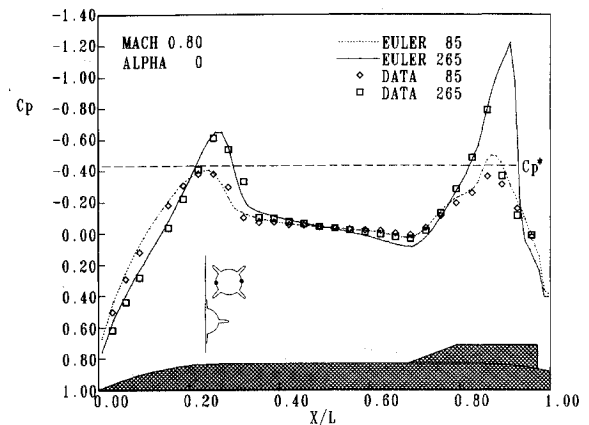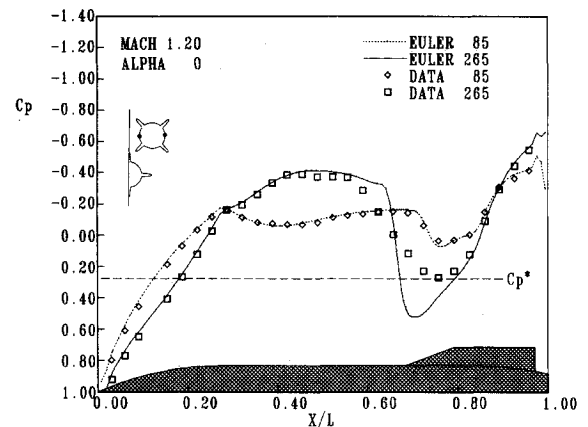
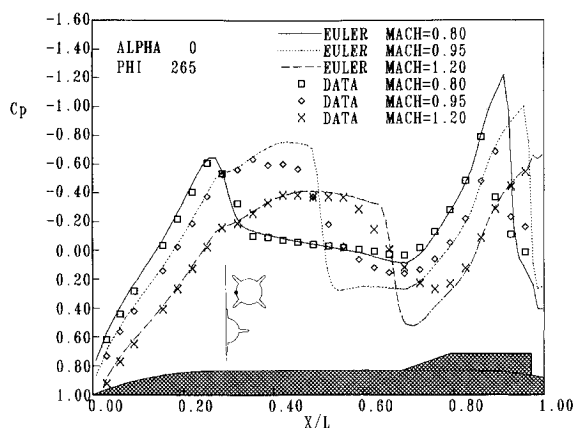Fig. 17   Supersonic interference effects, lower body

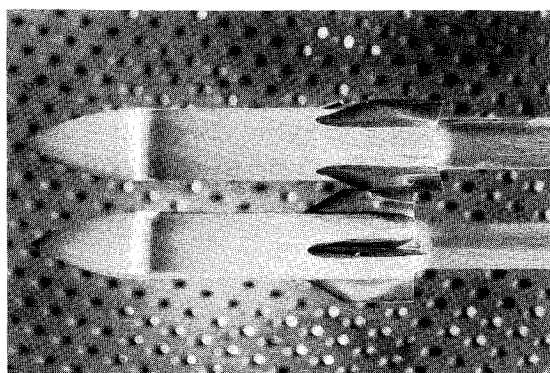**Fig. 18   Mach number effects, upper body, inboard side**

Fig. 19   Surface oil flow, Mach 0.80, $\alpha = 0$, 3-body case, side view
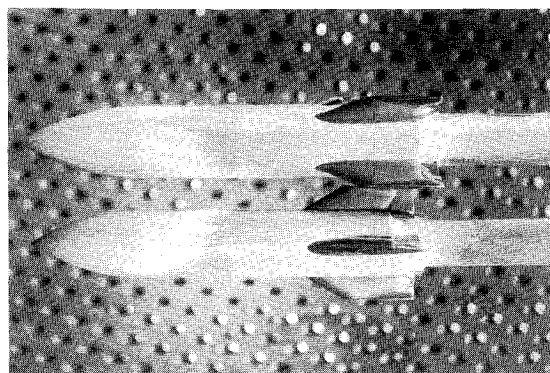

Fig. 20   Surface oil flow, Mach 0.95, $\alpha = 0$, 3-body case, side view
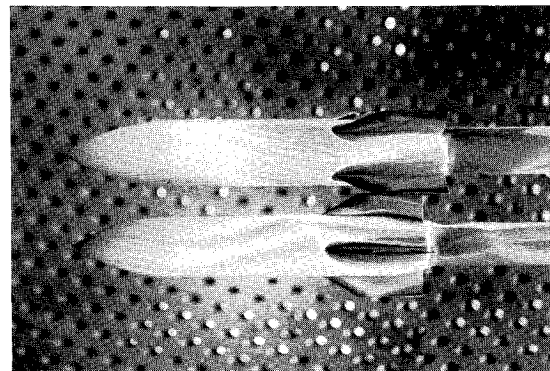

Fig. 21   Surface oil flow, Mach 1.20, $\alpha = 0$, 3-body case, side view

the fin leading-edge region. Unlike at Mach number 0.80 where little difference was observed across the body in the compression region after the body shock, a significant difference occurs here across the body, resulting in an outward force. Only the large expansion region prior to the shock on the inboard side, $X/L = 0.30$ to 0.60, serves to minimize the outward force. Again the identical behavior was seen on the upper/lower sides of the upper and lower bodies. Figure 17 supports this observation on the lower body and shows the good agreement between prediction and data and that was consistent throughout the investigation. Here the interference side prediction is at 30 deg clockwise from top center, while the minimum interference prediction is at 150 deg. The result is that at Mach 1.20, the resultant force is outward/upward on the upper body, and downward on the lower body.

Investigation of the moment coefficients yielded an equally interesting explanation. Figure 14 shows that the bodies react to the subsonic flow opposite to that in supersonic flow. Subsonically, the nose of each body moves away from the other, while the fin sections move toward each other. In supersonic flow the direct opposite occurs, where the body nose sections come together while the fin sections move apart. At Mach number 0.80, Fig. 15, the flow expansion on the inboard side of the upper body dominates the pitching and yaw moments. The difference across the fin section from outboard to inboard is so great that the fin sections move toward each other. Since this also occurs in the vertical plane of both the upper and lower bodies, the result is that the nose of the upper body pitches upward and yaws outboard, while the nose of the lower body pitches downward. This phenomena has been observed in flight on numerous occasions during subsonic carriage and release of multiple bodies from aircraft. Reversal of this trend supersonically can be explained from Figs. 16 and 17. The dominant feature here is the strong shock on the body at $X/L = 0.67$, with the accompanying expansion area before and sharp compression region after. This expansion/compression forms a couple that rotates the nose inward and the fin section outward. The magnitude of the moment is restricted by the proximity of the forces to the moment reference center, and the counteracting nose compression on the inboard side. Since the vertical plane of both the upper and lower bodies is similarly affected, the result is that the nose of the upper body pitches downward and yaws inward, while the nose of the lower body pitches upward.

The key element in establishing the observed multibody force and moment dependence on Mach number is the rearward movement of the body and fin region shocks, and elongation of the body flow expansion region. Figure 18 clearly illustrates this phenomena. The body shock near $X/L = 0.30$ for Mach 0.80 travels aft to $X/L = 0.50$ for Mach 0.95, and then to $X/L = 0.67$ for Mach 1.20. Meanwhile, the strong shock in the inboard fin region at Mach 0.80 moves off the body at Mach 1.20, leaving only an expansion region on the fins that was shown in Fig. 16 to have little influence. The rearward elongation of the body flow expansion region is evident in Fig. 18 and clearly depicted in surface oil flows, Figs. 19-21. The bright white region near the nose cylinder junction, Fig. 19, coincides with the expansion region at $X/L = 0.25$, Fig. 18. As the Mach increases to 0.95, the flow expansion region now elongates from $X/L = 0.25$ to 0.50, in Fig. 18. Figure 20 confirms the growing expansion region with the rearward movement of the bright oil concentration. A hint of the shock wave at $X/L = 0.50$ can be seen in the oil. This side view of the three-body configuration shows the inward movement of the oil toward the interference side of the bodies and the areas of lowest pressure. In Fig. 21, the shock has moved aft to the leading edge of the fins. The elongated expansion region upstream of the fins is clearly seen. By comparing the three oil flows, the shock in the fin region can be seen moving aft. At Mach 0.95, the shock is strong enough to induce a region of vorticity visible in the last quarter chord of the fins. Understandably, the Euler code was not able to capture this
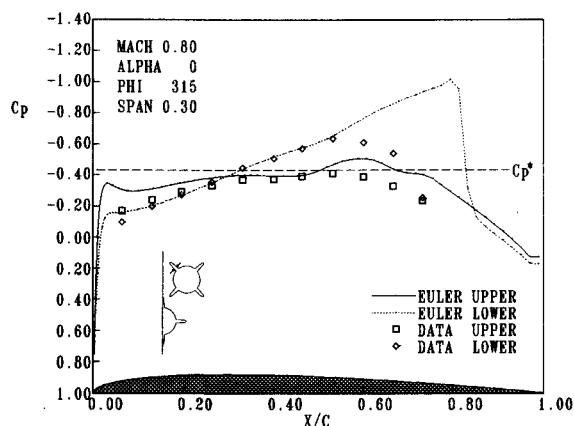
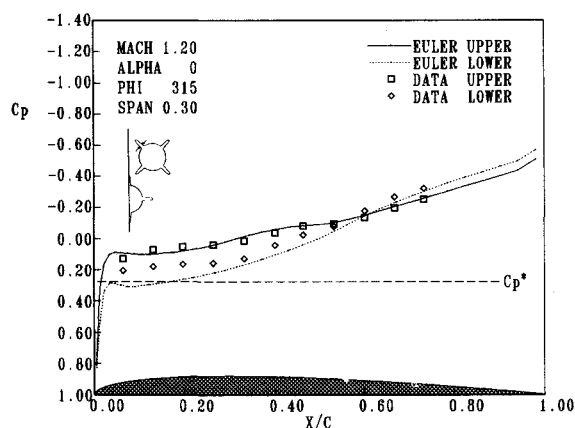**Fig. 22 Fin subsonic interference effects**

Fig. 23 Fin subsonic interference effects

region. The phenomena was very sensitive to the Mach number and interference flowfield in that it was only observed at Mach 0.95 and 1.05, and to various degrees of strength depending upon the fin orientation in the configuration, Fig. 20.

The rearward movement of the fin region shock is further illustrated in Figs. 22 and 23. Both figures show fin pressure distribution at 30% span on the 315-deg fin of the upper body. At Mach number 0.80, the shock is on the fin, although overpredicted and downstream of the data. Still, a clear, significant difference exists between the upper and lower surfaces, resulting in the inward/downward force as seen previously. Figure 23 shows the shock has moved off the fins and the differential between upper and lower surface pressures has lessened. This is consistent with the findings discussed earlier. These two figures are typical of the agreement between prediction and data on all of the fins.

Conclusions

Interference flow predictions were successfully made on multiple-body configurations in the transonic regime, where the strongest interference effects were found to exist near Mach 1. Agreement with data was very good in the minimum interference regions located on the outboard sides of the bodies. In the maximum interference regions between the bodies, the agreement with data was good in general, but shock location and structure were strongly influenced by viscous effects in the three-body case. It was found that the interference effects were not localized to the inboard sides of the bodies, but strongly influenced the expansion region and subsequent shock on the outboard sides. Consequently, the outboard sides of the bodies were not in a freestream condition. In addition, the prediction of fin pressures were found not as accurate as the predictions of body pressures.

It was also found that the force and moments on the three-body configuration were dependent on Mach number. This was primarily caused by the rearward movement of the expansion regions and subsequent shocks as the Mach number increased from 0.80–1.20. Subsonically, the net inboard forces in the dominant fin region resulted in nose-outward moments. At supersonic Mach numbers, the strengthening and movement of the body shock to just in front of the fins near the moment reference center resulted in an expansion/compression couple and nose-inward moments. These physical reactions to the interference flowfield, as well as the flowfield itself, were found to be adequately predicted by the Euler code. The dominant trends were predicted, although the details in the viscous regions were not.

References

[1]Thompson, J. F., "A Composite Grid Generation Code for General Three-Dimensional Regions—the EAGLE Code," *AIAA Journal,* Vol. 26, March 1988, pp. 271–272.

[2]Thompson, J. F., and Gatlin, B., "Program EAGLE User's Manual, Vol. II and III, Surface and Grid Generation Codes," AFATL-TR-88-117, Sept. 1988.

[3]Belk, D. M., and Whitfield, D. L., "Three-Dimensional Euler Solutions on Blocked Grids Using an Implicit, Two-Pass Algorithm," AIAA Paper 87-0450, Jan. 1987.

[4]Mounts, J. S., Belk, D. M., and Whitfield, D. L., "Program EAGLE User's Manual, Vol. IV, Multiblock, Implicit, Steady-State Euler Code," AFATL-TR-88-117, Sept. 1988.

[5]Lijewski, L. E., "Transonic Flow Solutions on a Blunt, Finned Body of Revolution Using the Euler Equations," AIAA Paper 86-1082, May 1986.

[6]Lijewski, L. E., "Transonic Flow Solutions on a Blunt, Body-Wing-Canard Configuration Using the Euler Equations," AIAA Paper 87-2273, Aug. 1987.

[7]Cottrell, C. J., Martinez, A., and Chapman, G. T., "A Study of Multibody Aerodynamic Interference at Transonic Mach Numbers," AIAA Paper 87-0519, Jan. 1987.

[8]Benek, J. A., Donegan, T. L., and Suhs, N. E., "Extended Chimera Grid Embedding Scheme with Application to Viscous Flows," AIAA Paper 87-1126, June 1987.

[9]Cottrell, C. J., and Lijewski, L. E., "Finned, Multibody Aerodynamic Interference at Transonic Mach Numbers," *Journal of Aircraft,* Vol. 25, Sept. 1988, pp. 827–834.

[10]Whitfield, D. L., and Janus, J. M., "Three-Dimensional Unsteady Euler Equations Solution Using Flux Vector Splitting," AIAA Paper 84-1552, June 1984.